Miniaturizable Phase-Sensitive Amplifier Based on Vector Dual-Pump Structure for Phase Regeneration of PDM Signal

Shuaiwei Jia , Zhuang Xie , Wen Shao, Xiaotian Han, Yulong Su, Jiacheng Meng, Duorui Gao, Wei Wang, and Xiaoping Xie

Abstract—Phase sensitive amplification is indispensable in promoting applications such as all-optical regenerators, quantum communications, all-optical analog-to-digital conversion, and long-distance communications. In this article, we proposed a vector dual-pump nondegenerate phase-sensitive amplification scheme based on ultra-silicon-rich nitride (Si_7N_3) waveguide, and theoretically verified its capability for all-optical regeneration of phase-encoded polarization-division multiplexing (PDM) signal without the need for complex polarization diversity structures. We achieved a gain extinction ratio (GER) of $\sim$37.5 dB by using a 3-mm-long Si_7N_3 waveguide with a high nonlinear coefficient ($\sim$279 /W/m). Signal quality before and after regeneration is characterized by constellation diagram and error vector magnitude (EVM). The results show that the EVM of the degraded PDM differential phase-shift keying (DPSK) signals with two polarization states of 54% and 53.8%, can be improved to 13.6% and 13.6%, respectively, after regeneration, directly illustrating the remarkable phase noise suppression effect. The applicability of the scheme in PDM quadrature phase shift keying (QPSK) signals was further investigated. Similarly, the EVMs of the two polarization states of the deteriorated QPSK signals are optimized from 28.9% and 29.3% to 13.7% and 13.9%, respectively. The proposed scheme has promising applications in integrated all-optical processing systems and long-distance transmission of optical communications.

Index Terms—Phase sensitive amplification, polarization-division multiplexing signals, all optical phase regeneration, nonlinear optical waveguide.

Shuaiwei Jia, Zhuang Xie, Wen Shao, Xiaotian Han, and Xiaoping Xie are with the State Key Laboratory of Transient Optics and Photonics, Xi'an Institute of Optics and Precision Mechanics, Chinese Academy of Sciences, Xi'an 710119, China, also with the School of Future Technology, University of Chinese Academy of Sciences, Beijing 100049, China, and also with the University of Chinese Academy of Sciences, Beijing 100049, China (e-mail: jiashuaiwei@opt.ac.cn; xiezhuang@opt.ac.cn; shaowen@opt.ac.cn; hanxiaotian@opt.ac.cn; xxp@opt.ac.cn).

Yulong Su is with the Department of Optoelectronic Engineering, Xidian University, Xi'an 710071, China (e-mail: ylsu@xidian.edu.cn).

Jiacheng Meng, Duorui Gao, and Wei Wang are with the State Key Laboratory of Transient Optics and Photonics, Xi'an Institute of Optics and Precision Mechanics, Chinese Academy of Sciences, Xi'an 710119, China (e-mail: mengjiacheng@opt.ac.cn; gaoduorui@opt.ac.cn; wangwei2012@opt.ac.cn).

I. INTRODUCTION

IN RECENT years, increasing attention has been paid to large-capacity transmission techniques as data traffic continuously expands. As an additional degree of freedom, the polarization state of the light can be used as a channel for signal multiplexing, thereby improving the capacity and spectral efficiency of the system [1]. Polarization Division Multiplexing (PDM) technology, which evolves by manipulating the polarization state of light, incorporates two linear and orthogonal polarization states within a single wavelength. In addition, PDM can be compatible with other multiplexing technologies, such as wavelength division multiplexing (WDM) [2], [3], [4], optical time division multiplexing [5], [6], mode division multiplexing [7] and space division multiplexing [8] systems to construct large-capacity, spectrally efficient communication systems. Nevertheless, it is inevitable that the phase encoded modulated signal based on the PDM technique is susceptible to disturbances from nonlinear phase noise that cannot be addressed by the normally digital signal processing methods during long distance transmission, which poses a critical challenge to the reliability of the received information [9], [10]. Therefore, it is urgent to enable nonlinear phase noise suppression using all-optical ways to improve the distance and fidelity of transmitted information. Fortunately, phase-sensitive amplifiers (PSAs) enable the compression of nonlinear phase noise owing to the in-phase and quadrature signal components experience unidentical gain [11], [12]. PSAs have attracted a wide range of researchers in recent years and has been implemented to squeeze the phase noise of diverse modulation formats, such as differential-phase-shift-keyed (DPSK) [11], [13], quadrature phase-shift-keyed (QPSK) [14], [15], and quadrature amplitude modulation [16], [17] signals.

Depending on the polarization state of the participating light waves, PSAs can be distinguished into scalar and vector types, and then further sub-divided into degenerated and non-degenerated PSAs according to the frequency relationship between the signal and the idler in the input waves [18], [19]. For the regeneration of PDM phase-encoded signals, without the employment of polarization diversity, only vector non-degenerated PSAs exhibit the ability to regenerate two polarization-states phase signals simultaneously. The majority of previous investigations focused on highly nonlinear optical fibers (HNLFs)

with a nonlinear refractive index of $n_2 = 2.6 \times 10^{-20}$ m^2/W, implying low nonlinearity, resulting in long interaction lengths (on the order of a few hundred meters), and pump power limited by stimulated Brillouin scattering (SBS) [20], [21], [22]. PSAs can also be implemented with other non-linear platforms such as periodically poled lithium niobate (PPLN) and Si-waveguide [23], [24], [25], [26]. The second-order nonlinear parametric process based on PPLN requires complex quasi-phase matching as well as being strongly sensitive to ambient temperature demanding precise temperature control, while PSAs based on Si-waveguide face large two-photon absorption (TPA), free-carrier absorption (FCA) and free-carrier dispersion (FCD) effects in the communication band restricting its regenerative performance. Although the nonlinear platform based on silicon nitride can accomplish no TPA, FCA, and FCD effects in the communication band [27], however, it has a moderate nonlinear coefficient, which means that longer waveguides are necessary to achieve high parametric amplification gains. Silicon nitride waveguides of 1.42 m have been reported [28]. but there are difficulties with the stitching technique of multiple spiral waveguides, resulting in poor waveguide yields. Meanwhile, silicon nitride with a standard stoichiometric ratio, which has higher strain, is prone to the problem of cracking [29]. Therefore, it is highly imminent to explore a phase regenerator based on a high-performance nonlinear integrated material to fulfill the phase regeneration of phase-encoded signals in PDM systems. The ultra-silicon-rich nitride (Si$_7$N$_3$) waveguide, as an CMOS-compatible nonlinear material platform, which provides the merits of high nonlinear refractive index ($n_2 = 2.8 \times 10^{-17}$ m^2/W), high bandgap energy, no TPA in the communication wavelength band, and meanwhile wide-band phase matching is available through dispersion-engineered waveguide design [30], [31]. Optical parametric amplification based on Si$_7$N$_3$ waveguides has been demonstrated by K.J.A. Ooi et al. [30]. Accordingly, we present for the first time a system scheme and theoretical simulation for realizing all-optical regeneration of PDM phase-coded signals based on Si$_7$N$_3$ waveguides.

This article is organized as follows: in Section II, the proposed black-box scheme for phase regeneration of PDM phase-encoded signals is established, and a four-wave mixing (FWM) coupled-wave model for phase regeneration of PDM signal in waveguide is developed. Then, the design of Si$_7$N$_3$ waveguide, the impact of key parameters affecting the regeneration effectiveness, including the signal-to-idler power ratio, the total pump power, and the signal power, and the results of PDM signal regeneration such as EVM, phase noise standard deviation, amplitude noise standard deviation, are included in Section III. A summary of the paper is presented in Section IV.

II. PHASE REGENERATION MODEL AND ANALYSIS BASED ON VECTOR PSA IN SI$_7$N$_3$ WAVEGUIDE

The proposed black-box system model for performing phase regeneration of the PDM phase-encoded signals is shown in Fig. 1(a), where the Si$_7$N$_3$ waveguide is served as a nonlinear medium to generate the phase-sensitive amplification process. The phase regeneration of PDM phase-encoded signals on the

basis of dual-pump nondegenerate vector PSA involves two fundamental conditions: 1). relative phase locking of the pump, signal and idler carriers [11], [19]; 2). The signal and idler in the input nonlinear medium are supposed to carry the identical phase information [32], [33]. Aiming to attain relative phase locking amongst interacting optical waves, a carrier recovery in combination with optical frequency comb generation can be adopted [11], [34], as shown in Fig. 1(a).

Due to the inherent frequency tooth coherence and large free spectrum range (FSR) of soliton microcavity combs (SMCs), it enables signal processing at high data rates that are not feasible with electro-optically modulated optical combs [35], [36], [37], [38], [39]. The idler, generated by the phase-insensitive FWM process, does not contain the data pattern, then the idler carrier is injected into the slave laser realizing the low-noise amplification of the idler carrier and finally injected into the high refractive index doped silica glass platform-based microring resonator to yield the SMC [35]. In order to satisfy that the signal and the idler carriers have the same phase information in the phase-sensitive amplification process, firstly, two specific frequency comb teeth are picked out as two pumps through the wavelength selection switch (WSS), and the coupler splits them into two paths and tunes them to orthogonal polarization states through the polarization controller (PC) and corresponds to each polarization component of the PDM signal, which subsequently undergoes a phase-insensitive Bragg scattering FWM process with the signal respectively [22], [40]. As a result, the idler is generated that carries the same phase information as the PDM signal light. Notably, we utilize HNLFs in carrier recovery and idler generation process in the schematic diagram of Fig. 1(a), which can be completely replaced in by Si$_7$N$_3$ waveguide if fabrication technology issues such as coupling loss, material loss, etc. are properly addressed. It is important to note that for the next step of the vector PSA process, the idler generated above need to be rotated separately to make its polarization states perpendicular to the corresponding PDM signal polarization component in the phase-insensitive process. Finally, the pumps are selected from the SMC through WSS for the vector PSA process, and the polarization states of the pumps are orthogonalized by PC in front of the polarization-maintaining fiber.

After the carrier recovery, injection locking and phase insensitive FWM process, the relative phase of the carriers is automatically locked among the signal, idler and pumps delivered to the Si$_7$N$_3$ waveguide. Meanwhile, a phase-locked loops used to compensate for carrier relative phase drift due to acoustic and thermal effects, as well as polarization tracking devices, are essential in practice to ensure optimal regeneration performance. It is worth emphasizing that our proposed scheme can operate as a black box because the phase-locked pumps and the idler are generated locally. Moreover, all components have the possibility of being replaced with on-chip integration in an attempt to meet future photonic integration demands for miniaturization, integration and low power consumption.

The vector dual-pump nondegenerate phase sensitive amplification process performed in the Si$_7$N$_3$ waveguide is shown in Fig. 1(b), where x, y denotes the two orthogonal polarization states of the interacting light waves. The red solid lines and
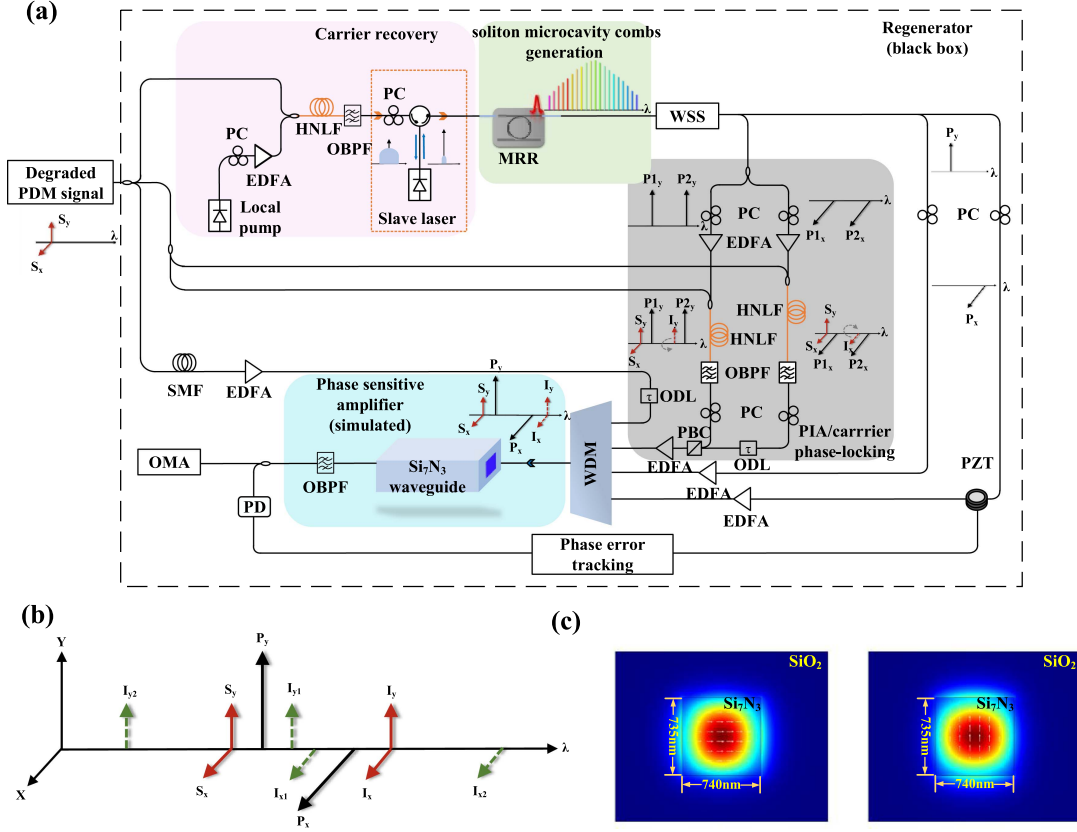
Fig. 1. (a) Schematic of miniaturizable regenerator including vector PSA based on Si_7N_3 waveguide, as well as carrier recovery, soliton microcavity combs generation, and PIA/carrier phase locking. In principle, carrier recovery is realized based on the injection locking process, the soliton microcavity combs is generated by feeding the pump arising from the carrier recovery into the microring resonator, the PIA process is used to generate carrier phase-locked pump, signal, and idler, the phase-sensitive amplification process takes place in the Si_7N_3 waveguide, where the simulation calculation is mainly focused on. PC: Polarization controller, HNLF: Highly nonlinear fiber, OBPF: Optical bandpass filter, MRR: Microring resonator, WSS: Wavelength selective switch, SMF: Single mode fiber, ODL: Optical delay line, PBC: Polarization beam combiner, WDM: Wavelength division multiplexer, PD: Photodetector, PZT: Piezoelectric-based fiber stretcher, OMA: Optical modulation analyzer. (b) Polarization and frequency diagram for vector dual-pump nondegenerate PSA processes for PDM phase regeneration. (c) Electric field intensity distribution of quasi-TE mode and quasi-TM mode of the Si_7N_3 waveguide at 1550 nm.

green dash lines represent the input light waves as well as the newly generated light waves, respectively. PDM signal S_x and S_y, the orthogonal pumps P_x and P_y, and idler I_x and I_y interact through two vector PSA processes, i.e., S_x-P_x-P_y-I_y and S_y-P_x-P_y-I_x, respectively. And the four newly generated waves, I_{x1}, I_{x2}, I_{y1}, I_{y2}, which are involved in four scalar FWM processes, i.e., S_x-P_x-I_{x2}, I_{x1}-P_x-I_x, S_y-P_y-I_{y1}, I_{y2}-P_y-I_y, respectively. [22], [30]. As previously mentioned, the polarization states of the above interacting light waves should be properly aligned. The Si_7N_3 waveguide is dispersion-engineered, and the effective refractive index n_{eff} and field distribution are calculated using the finite element method (FEM), and the material dispersion of silicon and Si_7N_3 is fitted by the

Sellmeier equations [30], [31], [41], [42]. The electric field profiles of the quasi-TE and quasi-TM mode of the Si_7N_3 waveguide at the telecommunication wavelength 1550 nm are shown in Fig. 1(c). A design with specific dimensions allows the effective refractive index of the TE and TM modes to approximate so that the polarization mode dispersion is negligible (see Section III).

For the purpose of theoretical study of the phase regeneration performance of the vector dual-pump nondegenerate phase sensitive amplification process based on Si_7N_3 waveguide, the four-wave mixing (FWM) coupled-wave model describing the vector phase sensitive amplification process in the waveguide is as follows:

$$
\frac{dA_{P_x}(z)}{dz} = -\left(\alpha_{P_x} + \alpha_{TPA,P_x} + \alpha_{FCA,P_x}\right) A_{P_x}(z) + i\gamma_{P_x}
$$

$$
\times \left[|A_{P_x}(z)|^2 + 2\left(|A_{S_x}(z)|^2 + |A_{I_x}(z)|^2 + |A_{I_{x1}}(z)|^2 + |A_{I_{x2}}(z)|^2\right)\right] A_{P_x}(z)
$$

$$
+ i\gamma_{P_x} \left[\frac{1}{3} \times 2\left(|A_{P_y}(z)|^2 + |A_{S_y}(z)|^2 + |A_{I_y}(z)|^2 + |A_{I_{y1}}(z)|^2 + |A_{I_{y2}}(z)|^2\right)\right] A_{P_x}(z)
$$

$$+ i2\gamma_{P_x} \times \frac{1}{3} \left(A_{P_y}(z)^* A_{I_x}(z) A_{S_y}(z) e^{\Delta\beta_{P_x, P_y, S_y, I_x} z} + A_{P_y}(z)^* A_{I_y}(z) A_{S_x}(z) e^{\Delta\beta_{P_x, P_y, S_x, I_y} z} \right)$$

$$+ i\gamma_{P_x} \left(A_{P_x}(z)^* A_{I_x}(z) A_{I_{x1}}(z) e^{\Delta\beta_{P_x, P_x, I_x, I_{x1}} z} + A_{P_x}(z)^* A_{S_x}(z) A_{I_{x2}}(z) e^{\Delta\beta_{P_x, P_x, S_x, I_{x2}} z} \right)$$

$$\frac{dA_{P_y}(z)}{dz} = - \left(\alpha_{P_y} + \alpha_{TPA, P_y} + \alpha_{FCA, P_y} \right) A_{P_y}(z)$$

$$+ i\gamma_{P_y} \times \left[|A_{P_y}(z)|^2 + 2 \left(|A_{S_y}(z)|^2 + |A_{I_y}(z)|^2 + |A_{I_{y1}}(z)|^2 + |A_{I_{y2}}(z)|^2 \right) \right] A_{P_y}(z)$$

$$+ i\gamma_{P_y} \left[\frac{1}{3} \times 2 \left(|A_{P_x}(z)|^2 + |A_{S_x}(z)|^2 + |A_{I_x}(z)|^2 + |A_{I_{x1}}(z)|^2 + |A_{I_{x2}}(z)|^2 \right) \right] A_{P_y}(z)$$

$$+ i2\gamma_{P_y} \times \frac{1}{3} \left(A_{P_x}(z)^* A_{I_x}(z) A_{S_y}(z) e^{\Delta\beta_{P_x, P_y, S_y, I_x} z} + A_{P_x}(z)^* A_{I_y}(z) A_{S_x}(z) e^{\Delta\beta_{P_x, P_y, S_x, I_y} z} \right)$$

$$+ i\gamma_{P_y} \left(A_{P_y}(z)^* A_{S_y}(z) A_{I_{y1}}(z) e^{\Delta\beta_{P_y, P_y, S_y, I_{y1}} z} + A_{P_x}(z)^* A_{I_y}(z) A_{I_{y2}}(z) e^{\Delta\beta_{P_y, P_y, I_y, I_{y2}} z} \right)$$

$$\frac{dA_{S_x}(z)}{dz} = - \left(\alpha_{S_x} + \alpha_{TPA, S_x} + \alpha_{FCA, S_x} \right) A_{S_x}(z)$$

$$+ i\gamma_{S_x} \times \left[|A_{S_x}(z)|^2 + 2 \left(|A_{P_x}(z)|^2 + |A_{I_x}(z)|^2 + |A_{I_{x1}}(z)|^2 + |A_{I_{x2}}(z)|^2 \right) \right] A_{S_x}(z)$$

$$+ i\gamma_{S_x} \left[\frac{1}{3} \times 2 \left(|A_{P_y}(z)|^2 + |A_{S_y}(z)|^2 + |A_{I_y}(z)|^2 + |A_{I_{y1}}(z)|^2 + |A_{I_{y2}}(z)|^2 \right) \right] A_{S_x}(z)$$

$$+ i2\gamma_{S_x} \times \frac{1}{3} A_{I_y}(z)^* A_{P_x}(z) A_{P_y}(z) e^{-\Delta\beta_{P_x, P_y, S_x, I_y} z} + i\gamma_{S_x} \times A_{I_{x2}}(z)^* A_{P_x}(z) A_{P_x}(z) e^{-\Delta\beta_{P_x, P_x, S_x, I_{x2}} z}$$

$$\frac{dA_{S_y}(z)}{dz} = - \left(\alpha_{S_y} + \alpha_{TPA, S_y} + \alpha_{FCA, S_y} \right) A_{S_y}(z)$$

$$+ i\gamma_{S_y} \times \left[|A_{S_y}(z)|^2 + 2 \left(|A_{P_y}(z)|^2 + |A_{I_y}(z)|^2 + |A_{I_{y1}}(z)|^2 + |A_{I_{y2}}(z)|^2 \right) \right] A_{S_y}(z)$$

$$+ i\gamma_{S_y} \left[\frac{1}{3} \times 2 \left(|A_{P_x}(z)|^2 + |A_{S_x}(z)|^2 + |A_{I_x}(z)|^2 + |A_{I_{x1}}(z)|^2 + |A_{I_{x2}}(z)|^2 \right) \right] A_{S_y}(z)$$

$$+ i2\gamma_{S_y} \times \frac{1}{3} \left(A_{I_x}(z)^* A_{P_x}(z) A_{P_y}(z) e^{-\Delta\beta_{P_x, P_y, S_y, I_x} z} \right) + i\gamma_{S_y} \left(A_{I_{y1}}(z)^* A_{P_y}(z) A_{P_y}(z) e^{-\Delta\beta_{P_y, P_y, S_y, S_y} z} \right)$$

$$\frac{dA_{I_x}(z)}{dz} = - \left(\alpha_{I_x} + \alpha_{TPA, I_x} + \alpha_{FCA, I_x} \right) A_{I_x}(z)$$

$$+ i\gamma_{I_x} \times \left[|A_{I_x}(z)|^2 + 2 \left(|A_{P_x}(z)|^2 + |A_{s_x}(z)|^2 + |A_{I_{x1}}(z)|^2 + |A_{I_{x2}}(z)|^2 \right) \right] A_{I_x}(z)$$

$$+ i\gamma_{I_x} \left[\frac{1}{3} \times 2 \left(|A_{P_y}(z)|^2 + |A_{S_y}(z)|^2 + |A_{I_y}(z)|^2 + |A_{I_{y1}}(z)|^2 + |A_{I_{y2}}(z)|^2 \right) \right] A_{I_x}(z)$$

$$+ i2\gamma_{I_x} \times \frac{1}{3} A_{S_y}(z)^* A_{P_x}(z) A_{P_y}(z) e^{-\Delta\beta_{P_x, P_y, I_x, S_y} z} + i\gamma_{I_x} \times A_{I_{x1}}(z)^* A_{P_x}(z) A_{P_x}(z) e^{-\Delta\beta_{P_x, P_x, I_{x1}, I_{x1}} z}$$

$$\frac{dA_{I_y}(z)}{dz} = - \left(\alpha_{I_y} + \alpha_{TPA, I_y} + \alpha_{FCA, I_y} \right) A_{I_y}(z)$$

$$+ i\gamma_{I_y} \times \left[|A_{I_y}(z)|^2 + 2 \left(|A_{P_y}(z)|^2 + |A_{S_y}(z)|^2 + |A_{I_{y1}}(z)|^2 + |A_{I_{y2}}(z)|^2 \right) \right] A_{I_y}(z)$$

$$+ i\gamma_{I_y} \left[\frac{1}{3} \times 2 \left(|A_{P_x}(z)|^2 + |A_{S_x}(z)|^2 + |A_{I_x}(z)|^2 + |A_{I_{x1}}(z)|^2 + |A_{I_{x2}}(z)|^2 \right) \right] A_{I_y}(z)$$

$$+ i2\gamma_{I_y} \times \frac{1}{3} \left(A_{S_x}(z)^* A_{P_x}(z) A_{P_y}(z) e^{-\Delta\beta_{P_x, P_y, I_y, S_x} z} \right) + i\gamma_{I_y} \left(A_{I_{y2}}(z)^* A_{P_y}(z) A_{P_y}(z) e^{-\Delta\beta_{P_y, P_y, I_{y2}, I_{y2}} z} \right)$$

$$
\begin{aligned}
\frac{dA_{I_{x1}}(z)}{dz} = {}& -\left(\alpha_{I_{x1}} + \alpha_{TPA,I_{x1}} + \alpha_{FCA,I_{x1}}\right) A_{I_{x1}}(z) + i\gamma_{I_{x1}} \\
& \times \left[|A_{I_{x1}}(z)|^2 + 2\left(|A_{P_x}(z)|^2 + |A_{s_x}(z)|^2 + |A_{I_x}(z)|^2 + |A_{I_{x2}}(z)|^2 \right) \right] A_{I_{x1}}(z) \\
& + i\gamma_{I_{x1}} \left[\frac{1}{3} \times 2\left(|A_{P_y}(z)|^2 + |A_{S_y}(z)|^2 + |A_{I_y}(z)|^2 + |A_{I_{y1}}(z)|^2 + |A_{I_{y2}}(z)|^2 \right) \right] A_{I_{x1}}(z) \\
& + i\gamma_{I_{x1}} \times A_{I_x}(z)^* A_{P_x}(z) A_{P_x}(z) e^{-\Delta\beta_{P_x, P_x, I_x, I_x} z}
\end{aligned}
$$

$$
\begin{aligned}
\frac{dA_{I_{y1}}(z)}{dz} = {}& -\left(\alpha_{I_{y1}} + \alpha_{TPA,I_{y1}} + \alpha_{FCA,I_{y1}}\right) A_{I_{y1}}(z) + i\gamma_{I_{y1}} \\
& \times \left[|A_{I_{y1}}(z)|^2 + 2\left(|A_{P_y}(z)|^2 + |A_{S_y}(z)|^2 + |A_{I_y}(z)|^2 + |A_{I_{y2}}(z)|^2 \right) \right] A_{I_{y1}}(z) \\
& + i\gamma_{I_{y1}} \left[\frac{1}{3} \times 2\left(|A_{P_x}(z)|^2 + |A_{S_x}(z)|^2 + |A_{I_x}(z)|^2 + |A_{I_{x1}}(z)|^2 + |A_{I_{x2}}(z)|^2 \right) \right] A_{I_{y1}}(z) \\
& + i\gamma_{I_{y1}} \left(A_{s_y}(z)^* A_{P_y}(z) A_{P_y}(z) e^{-\Delta\beta_{P_y, P_y, I_{y1}, S_y} z} \right)
\end{aligned}
$$

$$
\begin{aligned}
\frac{dA_{I_{x2}}(z)}{dz} = {}& -\left(\alpha_{I_{x2}} + \alpha_{TPA,I_{x2}} + \alpha_{FCA,I_{x2}}\right) A_{I_{x1}}(z) + i\gamma_{I_{x2}} \\
& \times \left[|A_{I_{x2}}(z)|^2 + 2\left(|A_{P_x}(z)|^2 + |A_{s_x}(z)|^2 + |A_{I_x}(z)|^2 + |A_{I_{x1}}(z)|^2 \right) \right] A_{I_{x2}}(z) \\
& + i\gamma_{I_{x2}} \left[\frac{1}{3} \times 2\left(|A_{P_y}(z)|^2 + |A_{S_y}(z)|^2 + |A_{I_y}(z)|^2 + |A_{I_{y1}}(z)|^2 + |A_{I_{y2}}(z)|^2 \right) \right] A_{I_{x2}}(z) \\
& + i\gamma_{I_{x2}} \times A_{S_x}(z)^* A_{P_x}(z) A_{P_x}(z) e^{-\Delta\beta_{P_x, P_x, I_{x2}, S_x} z}
\end{aligned}
$$

$$
\begin{aligned}
\frac{dA_{I_{y2}}(z)}{dz} = {}& -\left(\alpha_{I_{y2}} + \alpha_{TPA,I_{y2}} + \alpha_{FCA,I_{y2}}\right) A_{I_{y2}}(z) + i\gamma_{I_{y2}} \\
& \times \left[|A_{I_{y2}}(z)|^2 + 2\left(|A_{P_y}(z)|^2 + |A_{S_y}(z)|^2 + |A_{I_y}(z)|^2 + |A_{I_{y1}}(z)|^2 \right) \right] A_{I_{y2}}(z) \\
& + i\gamma_{I_{y2}} \left[\frac{1}{3} \times 2\left(|A_{P_x}(z)|^2 + |A_{S_x}(z)|^2 + |A_{I_x}(z)|^2 + |A_{I_{x1}}(z)|^2 + |A_{I_{x2}}(z)|^2 \right) \right] A_{I_{y2}}(z) \\
& + i\gamma_{I_{y2}} \left(A_{I_y}(z)^* A_{P_y}(z) A_{P_y}(z) e^{-\Delta\beta_{P_y, P_y, I_{y2}, I_y} z} \right)
\end{aligned}
\tag{1}
$$

where A_i $(i) = \sqrt{P_i(z)}\, e^{i\phi_i(z)}$ is the complex amplitude of the optical field, $P_i(z)$ and $\phi_i(z)$ are the power and phase of the optical wave varying with the length of the waveguide, α_i, $\alpha_{FCA,i}$, $\alpha_{TPA,i}$ represent the linear transmission loss, FCA loss and TPA loss in the waveguide, respectively. It should be noted that the Si_7N_3 waveguide has no TPA and FCA effects in the communication band, so we have neglected them in our later simulations. γ_i is the nonlinear coefficient of the waveguide at different wavelengths. A total of 10 waves shown in Fig. 1(b) involved in the interaction are under consideration as mentioned before. $\omega_a + \omega_b = \omega_c + \omega_d$ and $2\omega_p = \omega_o + \omega_q$ denote the vector dual-pump FWM and scalar single-pump FWM processes, respectively. ω is the angular frequency of the light wave, and the corresponding subscripts a, b, c, d and p, q, o correspond to each wave participating in different vector and scalar FWM processes, respectively (e.g., for the vector FWM process, S_x-P_x-P_y-I_y, a, b, c, d represent P_x, P_y, I_y, S_x, respectively; for the scalar FWM process, S_x-P_x-I_{x2}, p, q, o stands for P_x, I_{x2}, S_x, respectively); In terms of orthogonal polarization states, the vector FWM has a nonlinear coefficient which is 2/3 of that of the scalar single-pump FWM. Meanwhile, the cross-phase modulation (XPM) between the cross-polarized waves has a nonlinear coefficient which is 1/3 of that of the XPM between the co-polarized waves. $\Delta \beta_{a,b,c,d} = \beta_a + \beta_b - \beta_c - \beta_d$ and β_i are the linear wave vector mismatch and propagation constant of each light wave, respectively. SBS and stimulated Raman scattering (SRS) effects are neglected on account of the short length of the waveguide [43], [44]. Besides, only dominating FWM processes are considered in the calculation of (1) shown at the bottom of previous page for the simplification, which would not have significant influences on the results [22], [45].

In purpose of evaluating the capability of our proposed scheme for PDM signal regeneration, in the following sections, we performed a detailed investigation of the Si_7N_3 waveguide design, the factors affecting the gain extinction ratio (GER) (i.e., the total pump power P_{pumps}, the signal power P_{signal}, signal-to-idler power ratio σ), and the regeneration performance of PDM DPSK and PDM QPSK signals.
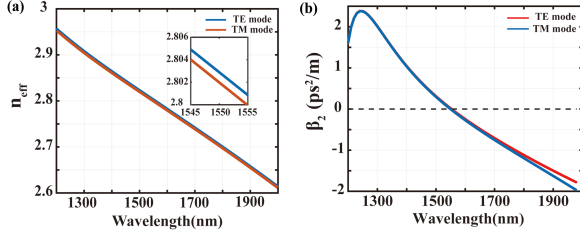
Fig. 2. (a) Effective refractions of the TE and TM mode as a function of the wavelength. Inset: zoom-in profile of effective refraction of the Si_7N_3 waveguide. (b) Polarization mode dispersion profiles of the Si_7N_3 waveguide.
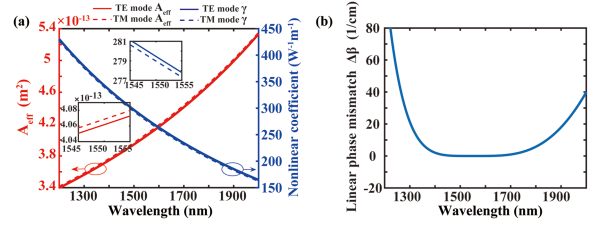

Fig. 3. (a) Curves of effective mode area and nonlinear coefficient as functions of wavelength. (b) Linear phase mismatches as functions of the wavelength.

III. SIMULATION AND DISCUSSION

A. Design of the Si_7N_3 Waveguide

Si_7N_3 as a third-order nonlinear medium, which exhibits the merits of high Kerr nonlinearity, low loss (4.5 dB/cm), large band gap (2.1 eV) and compatibility with the CMOS (has the capability of large-scale manufacturing) [30], [31], [46], [47]. By utilizing FEM, we obtained the effective mode refractive index n_{eff} and field distribution of the Si_7N_3 waveguide, and achieved a second-order dispersion of 0 near 1550 nm with the optimization of the waveguide dimensions (W = 740 nm, H = 735 nm, waveguide length = 3 mm) (the second-order dispersion is calculated by $\beta_2 = d^2\beta/d\omega^2$, $\beta = 2\pi n_{eff}/\lambda$). It should be remarked that we utilize only the fundamental modes (TE_{00}/TM_{00}) of the designed waveguide in the following analysis, without considering the higher order modes. The dependence of n_{eff} with wavelength for the quasi-TE and quasi-TM modes is shown in Fig. 2(a), and the inset of Fig. 2(a) shows the n_{eff} around 1550 nm. Fig. 2(b) illustrates the second-order dispersion of the waveguide, and it is revealed that the dispersions of the TE and TM modes are approximately identical, which means that the PMD is negligible in our scheme.

The effective mode area A_{eff} and the nonlinear coefficient γ of the designed Si_7N_3 waveguide are calculated as follows:

$$A_{eff} = \frac{\left(\iint |F(x,y)|^2 dx dy\right)^2}{\iint |F(x,y)|^4 dx dy} \tag{2}$$

$$\gamma = \frac{2\pi}{\lambda} \frac{\iint n_2(x,y)|F(x,y)|^4 dx dy}{\left(\iint |F(x,y)|^2 dx dy\right)^2} \tag{3}$$

where $F(x,y)$ is the electric field distribution, λ is the wavelength of the light wave, and n_2 is the nonlinear refractive index of Si_7N_3. The variation of A_{eff} and nonlinear coefficients γ versus wavelength for the quasi-TE and quasi-TM modes are shown in Fig. 3(a), where it can be observed that the A_{eff} increases with wavelength while γ is reversed, and the A_{eff} and γ at 1550 nm are $4.07 \times 10^{-13}\ m^2$ and 279 /W/m, respectively. Notably, the nonlinearity coefficient of Si_7N_3 is five orders of magnitude higher than that of HNLFs ($\sim$0.02 /W/m). Highly efficient FWM processes need to fulfill the phase matching condition, and Fig. 3(b) shows the linear phase mismatch for wavelengths from 1200 nm to 2000 nm. It can be noticed that the dispersion curves for quasi-TE and quasi-TM modes

are nearly zero at 1550 nm, while the linear phase mismatch (calculated by $\Delta\beta_{a,b,i,c} = \beta_a + \beta_b - \beta_i - \beta_c$) is flat and small in the 1400 nm–1800 nm, which guarantees the efficiency of the FWM process. The broadband phase matching and considerable nonlinear coefficients ensure that our scheme provides a high gain-to-extinction ratio over a wide wavelength range. Furthermore, since the carrier phase-locked pump light in our proposed scheme originates from an optical frequency comb, its exploitable wavelength is undoubtedly ultra-broadband. Thereby a further extension is that our proposed scheme has excellent wavelength scalability and flexibility. In conclusion, our proposed Si_7N_3 waveguide is quite suitable for vector dual pump nondegenerate PSA, and subsequently its phase-sensitive gain properties should be optimized.

B. Gain Extinction Ratio Characterization

GER, defined as the ratio of phase-sensitive amplification to de-amplification, is an important indicator to assess the phase regeneration capability of PSA [48]. In our calculations utilizing (1), the parameters of the Si_7N_3 waveguide are as follows: the waveguide length L = 3 mm, and the dispersion slope, fourth-order dispersion coefficient, and nonlinear coefficient at 1550 nm are 4.3×10^{-6} ps/nm²/km, 7.365×10^{-6} ps⁴/km, and 279 /W/km, respectively. At the input of the Si_7N_3 waveguide, two continuous waves with the equal power and wavelengths of 1540 nm and 1560 nm, respectively, are treated as orthogonal pumps, where $\gamma_{p_x} = 282.3$ /W/km, $\gamma_{p_y} = 275.6$ /W/km, $A_{eff,P_x} = 4.04 \times 10^{-13}\ m^2$, $A_{eff,P_y} = 4.08 \times 10^{-13}\ m^2$. The PDM signal's wavelength is 1537.5 nm, for simplicity, the power of both polarization components is 10 dBm, and carry equal phase information in the simulation, $\gamma_{s_{x,y}} = 285.7$ /W/km, $A_{eff,s_{x,y}} = 4.02 \times 10^{-13}\ m^2$, correspondingly, the idler's wavelength is 1562.5 nm and is set in the simulation to have the same phase information as the corresponding signal, $\gamma_{I_{x,y}} = 275.4$ /W/km, $A_{eff,I_{x,y}} = 4.07 \times 10^{-13}\ m^2$. $\alpha_i = 4.5$ dB/cm account for the linear losses.

Normally, the power of signal and idler in scalar PSA is identical. However, as we have shown in Fig. 1(a), the idler involved in the PSA process is actually generated through the FWM process in HNLFs, whose power is limited by the efficiency of the FWM process as well as the power of the signal involved in the interaction. Therefore, it is necessary to analyze the effect of the GER caused by different signal-to-idler power ratios when performing the PSA process in Si_7N_3 waveguides, taking into account the idler power issues arising from the actual
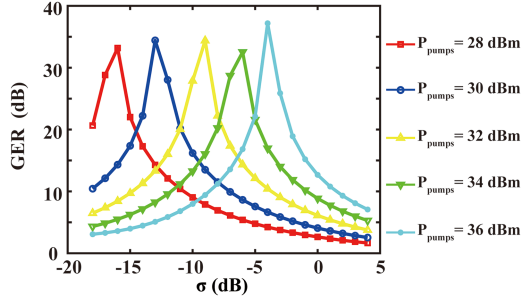
Fig. 4. Calculated signal gain extinction ratio (GER) for the x-pol component of the PDM DPSK signal as a function of the input signal-to-idler ratio σ for different total pump power, P_{pumps}, i.e., $P_{pumps} = 28, 30, 32, 34$ and 36 dBm.
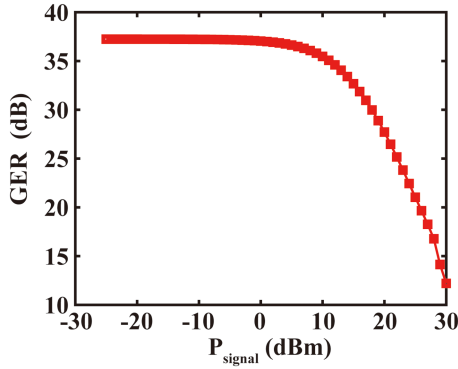

Fig. 5. Calculated signal gain extinction ratio (GER) as a function of the signal power, P_{signal}, for x-pol component of the PDM DPSK signal, with total pumps power $P_{pumps} = 36$ dBm, signal-to-idler power ratio $\sigma = -4$ dB.

process. Thus, we first optimize the signal-to-idler power ratio σ. The GER of one PDM DPSK component (x-pol) is shown in Fig. 4. The result of the other PDM component (y-pol) is quite the same as the result of x-pol, so we only focus on the result of x-pol for analysis here. It can be seen that the optimal σ exists for different pump power, and it grows with the increase of P_{pumps}. A large σ is preferred, as the idler power is restricted by the signal. Consequently, a σ of -4 dB is selected for $P_{pumps} = 36$ dBm, with $P_{signal} = 10$ dBm/polarization, and $P_{idler} = 14$ dBm/polarization. The corresponding GER is about 37.5 dB. It should be remarked that the HNLFs shown in Fig. 1(a) for generating carrier phase-locked idler can be replaced by Si_7N_3 owing to its higher nonlinear coefficient as well as the potential to engineer the dispersion so as to achieve broader bandwidth phase matching to achieve more efficient FWM conversion efficiency, which in turn generates higher-power idler to satisfy the desired signal-to-idler power ratio. In this way, the footprint of the whole system is further minimized.

One of the challenges of PSA for phase regeneration of degraded signals is that PSA causes an increase in amplitude noise (AN) while reducing the phase noise (PN) [11], [49], due to the intrinsic gain curve of PSA. Fortunately, AN can be somewhat suppressed by keeping the PSA operating in the gain saturation region [11], [45], a process that can be implemented by increasing the signal optical power or preventing the use of higher pump power. Fig. 5 indicates the GER of the signal changes with the
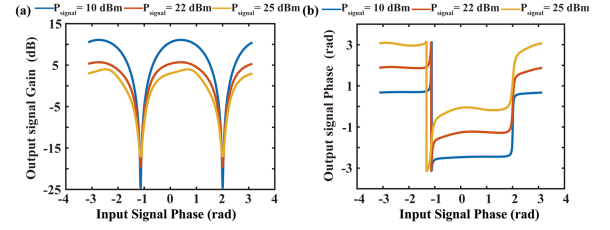

Fig. 6. (a) Gain and (b) phase of the output signal as a function of input signal phase for x-pol component of the PDM DPSK signal, with total pumps power $P_{pumps} = 36$ dBm, signal-to-idler power ratio $\sigma = -4$ dB.

P_{signal}. Similarly, for the x-pol and y-pol components of the PDM signal, their results are highly similar, and we focus on the x-pol component as well. As can be seen, when the P_{signal} is larger than 10 dBm/polarization, GER gradually falls with the growth of P_{signal} due to the gain saturation effect. A well balanced P_{signal} is required to ensure step-like phase transfer function and saturation gain transfer function simultaneously for better regeneration performance.

Based on the above analysis, we selected three P_{signal} in the GER saturation region, $P_{signal} = 10$ dBm/polarization, $P_{signal} = 22$ dBm/polarization and $P_{signal} = 25$ dBm/polarization, to investigate the transfer function characteristics of the vector PSA, as shown in Fig. 6. Fig. 6(a) and (b) represent the gain and phase transfer functions of the x-pol component of the PDM DPSK signal, respectively. Apparently, as the P_{signal} rises, the extent of saturation increases. Nevertheless, oversaturation leads to an uneven gain curve and distortion of the step-like phase transfer curve. Therefore, it is more desirable to select a suitable P_{signal} so that the vector PSA works in the moderate saturation region to allow a trade-off between output amplitude and phase. Therefore, the P_{signal} is fixed to 22 dBm/polarization for the PDM signal phase regeneration.

C. Phase Regeneration of PDM DPSK Signals

We further demonstrate the phase regeneration effectiveness of the PDM DPSK signals based on our proposed scheme. Based on the optimization results in the previous sections, the power of the pump, signal, and idler we used in the simulation is 36 dBm, 22 dBm/polarization, and 26 dBm/polarization, respectively. For more generality, we assume that all light waves used are continuous and consider that the complex amplitudes of their light fields exhibit the form $A = \sqrt{P} e^{i\varphi}$. Assuming that the phases of both polarization components of the PDM signal are independently modulated to a random 0, π phase distribution at 40 Gbit/s in the DPSK format, generating the 80 Gbit/s PDM signal, and are subsequently degraded by PN and AN which following random distributions with standard deviations of 1.09 rad and 0.173, respectively. The signal with noise is $A = (A_0 + A_n)e^{i(\varphi_0 + \varphi_n)}$, where $\varphi_0 = 0$, π, and φ_n is PN, A_n is AN, and the signal after regeneration is $A = \sqrt{G(\varphi_n)}(A_0 + A_n)e^{i(\varphi_0)}$. We simulated the proposed phase signals regeneration scheme based on MATLAB using 1×10^7 bits of data. The simulation results are illustrated in Fig. 7. As shown in Fig. 7(a) and (b) the PN distribution of
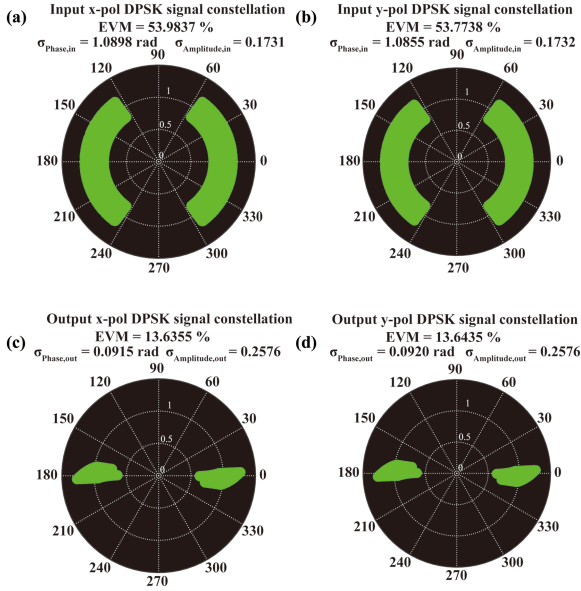
Fig. 7. Simulated constellation of PDM DPSK signals: (a) x-pol signal without PSA; (b) y-pol signal without PSA; (c) regenerated x-pol signal; (d) regenerated y-pol signal.
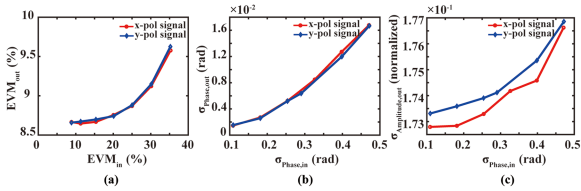

Fig. 8. (a) EVM of the PDM DPSK signals before and after phase regeneration. (b) The calculated plots of output phase standard deviation $\sigma_{phase,in}$. (c) The calculated plots of output amplitude standard deviation $\sigma_{amplitude,out}$.

each polarization component is about 2.02 rad, after regeneration the PN of output signal does not exceed 0.35 rad, as shown in Fig. 7(c) and (d), a significant PN squeeze effect can be observed by comparing the input and output constellations. The AN is also suppressed owing to the PSA operating in the saturation region. As an intuitive observation of the performance of phase regeneration, we measured the EVMs of the PDM DPSK signals before and after regeneration, which is defined as follows [50]:

$$\text{EVM} = \left(\frac{1}{2} \sum_{i=1}^{I} |E_{r,i} - E_{t,i}| \right)^{1/2} \Big/ |E_{t,m}| \qquad (4)$$

where $E_{r,i}$ and $E_{t,i}$ are actually the received signal vector and ideal transmitted signal vector, respectively, $|E_{t,m}|$ is the power of the longest ideal constellation vector, which serves for normalization, and I is the bit length of the signal data. The EVMs effectively measure the error distance of the received signal from its ideal position. The EVMs of the two components of the degraded PDM signal are 54% and 53.78% respectively, and after vector PSA their EVMs are optimized to 13.64% and 13.64%, respectively.

As shown in Fig. 8(a), to evaluate the tolerance of phase regeneration of the proposed scheme, we quantitatively compare

the EVMs of the PDM signal with different levels of deterioration before and after regeneration. The results reveal that the EVMs of the regenerated PDM signal are much smaller than the input degraded PDM signal, which implies that the vector dual-pump PSA based on Si_7N_3 waveguide has excellent PN and AN compression capability. Furthermore, to quantify the phase regeneration performance more thoroughly, the PSA is evaluated in terms of phase and amplitude variance, as shown in Fig. 8(b) and (c). Fig. 8(b) is the calculated output phase standard deviation $\sigma_{phase,out}$ as a function of the input phase standard deviation $\sigma_{phase,in}$. The reduction of $\sigma_{phase,out}$ by one order of magnitude for all cases indicates that the phase compression is effective at different PN levels. Fig. 8(c) depicts a curve of the output amplitude standard deviation $\sigma_{amplitude,out}$ with the signal amplitude normalized to 1. The results show that a fairly minor PN-AN conversion exists at different PN levels. When $\sigma_{phase,in}$ exceeds to 0.5 rad, $\sigma_{amplitude,out}$ increases by only 1.9%. Although a degree of amplitude jitter is introduced, the signal EVM is significantly improved after regeneration.

D. Phase Regeneration of PDM QPSK Signals

The PDM QPSK signals double the spectral efficiency compared to the PDM DPSK signals, which represents a twofold increase in information capacity and is the recommended communication format for current networks [51], [52]. Therefore, we further investigated the phase regeneration of the PDM QPSK signals. Phase regeneration of QPSK signals requires a four-order staircase-like phase transfer function, which can be realized by signal interfering with the conjugated third-phase harmonic [14] or by a dual-conjugate-pump degenerate PSA [53]. This means that the second pump demands a high-order FWM process to generate the fourth harmonic of phase to achieve modulation stripping. The realization of third-order harmonics may be challenging for a practically experimental system, and based on a higher-order FWM process is a considerable solution towards this problem [14]. In the simulation, for simplicity, the phase information on the idler involved in the PSA process is set to be three times that of the corresponding input signal. The power optimization process for pump, signal, and idler is similar to the optimization process for phase regeneration of PDM DPSK signal. The GER of one PDM QPSK component (x-pol) for different total pump power is shown in Fig. 9. The wavelength and power of the PDM QPSK signal used in the simulation are the same as those of the PDM DPSK signal, which are 1537.5 nm and 10 dBm/polarization, respectively.

It is worth noting that in the process of PDM-QPSK regeneration, it does not mean that the larger GERs the better, the larger GERs will actually lead to the four-order staircase-like phase transfer function heavy distortions and fail to realize the phase compression of the QPSK signal [14]. Therefore, in the simulation the signal-to-idler ratio is set to $\sigma = 5$ dB to achieve the desired phase regeneration effect. Fig. 10 indicates the GER of the signal changes with the P_{signal} for x-pol component of the PDM QPSK signal. The total pumps power is 36 dBm. The GER achieved in the PSA process is ~7 dB.
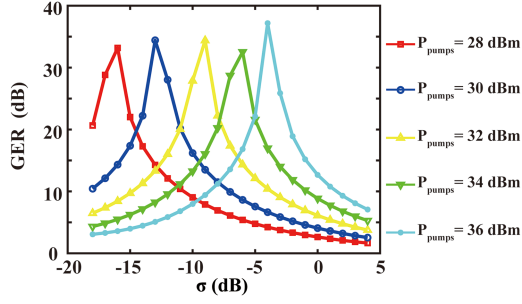
Fig. 9. Calculated signal gain extinction ratio (GER) for the x-pol component of the PDM QPSK signal as a function of the input signal-to-idler ratio σ for different total pump power, P_{pumps}, i.e., $P_{pumps} = 28, 30, 32, 34$ and 36 dBm.
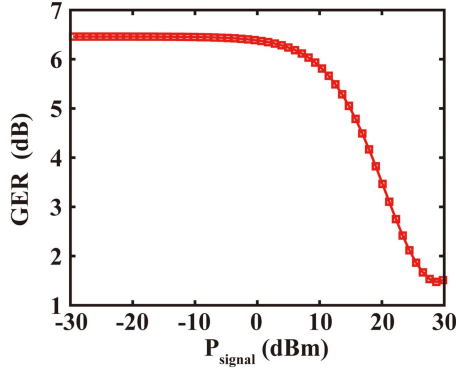

Fig. 10. Calculated signal gain extinction ratio (GER) as a function of the signal power for x-pol component of the PDM QPSK signal, P_{signal}, with total pumps power $P_{pumps} = 36$ dBm, signal-to-idler power ratio $\sigma = 5$ dB.
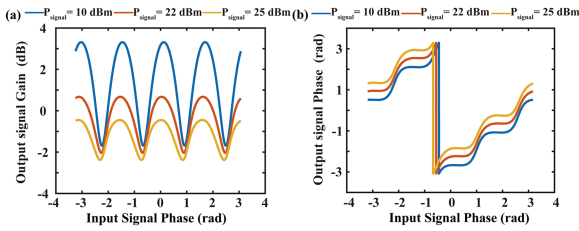

Fig. 11. (a) Gain and (b) phase of the output signal as a function of input signal phase for x-pol component of the PDM QPSK signal, with total pumps power $P_{pumps} = 36$ dBm, signal-to-idler power ratio $\sigma = 5$ dB.

Similarly, in order to minimize the PN-AN transition, we simulate to investigate the gain and phase transfer function curves of the PDM-QPSK signal for the gain saturation case. Fig. 11(a) shows the power transfer function curve of the x-pol component of the PDM QPSK signal, similar to Fig. 6(a), with the distinction that the phase-sensitive gain period is reduced to half. As shown in Fig 11(b), the phase transfer function curve exhibits a fourth-order step shape different from that of Fig. 6(b).

Consequently, we simulate the pump, signal, and idler with power of 33 dBm/polarization, 22 dBm/polarization, and 17 dBm/polarization, respectively, which means a σ of 5 dB is selected. Similarly, in the simulation, both polarization components of the PDM QPSK signal are independently modulated with different phase information in QPSK format at 40 Gbit/s and subsequently distorted by adding the PN and AN, generating the 80 Gbit/s PDM QPSK signal. We emulated the phase
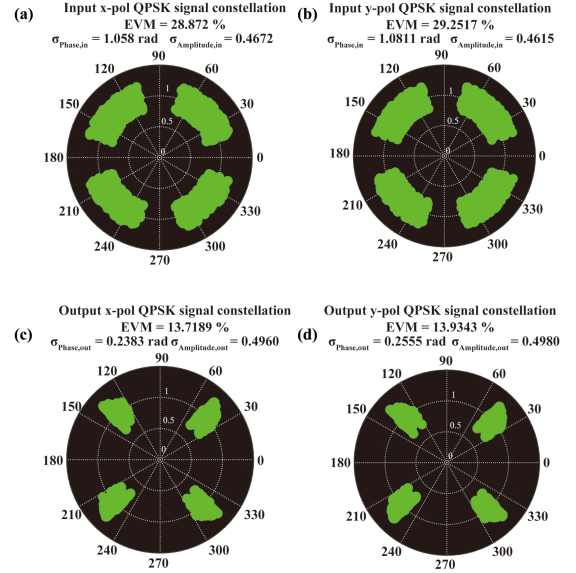

Fig. 12. Simulated constellation of PDM QPSK signals: (a) x-pol signal without PSA; (b) y-pol signal without PSA; (c) regenerated x-pol signal; (d) regenerated y-pol signal.
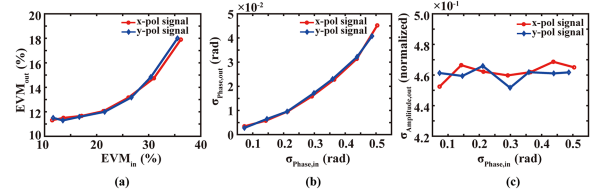

Fig. 13. (a) EVM of the PDM DPSK signals before and after phase regeneration. (b) The calculated plots of output phase standard deviation $\sigma_{phase,out}$. (c) The calculated plots of output amplitude standard deviation $\sigma_{amplitude,out}$.

regeneration scheme for the PDM QPSK phase-encoded signal using 1×10^7 bits of data similarly. The simulation results of the constellations are shown in Fig. 12. Similar to Fig. 7, it is intuitive to exhibit the compression performance of the PN of the PDM QPSK signal after phase regeneration. The EVMs of the distorted PDM QPSK signal are 28.87% and 29.25% for x-pol and y-pol, respectively, and after regeneration the EVMs are improved to 13.72% and 13.93%, respectively. The EVM of the output PDM QPSK signals as a function of the input PDM QPSK signals EVM is illustrated in Fig. 13(a), also exhibits high tolerance for phase compression. Likewise, the output signal standard deviation $\sigma_{phase,out}$ presents an order of magnitude improvement, while the difference is that for QPSK signals, the increase in $\sigma_{amplitude,out}$ due to PN-AN conversion is less noticeable. We attribute this mainly to the gain saturation operation and the lower GER characteristic of QPSK regeneration process, as well as the lower absolute phase noise which can be exercised with QPSK signal. The effective compression of different levels of PN provided by the regenerator is fully confirmed.

As a summary of the above analysis, it could be concluded that a dependence exists between phase regeneration performance and GER. The analytic solution for the gain of a double-pumped PSA, without considering the pump light consumption and with

TABLE I
COMPARISON OF DIFFERENT NONLINEAR MATERIALS USED FOR NONLINEAR PHOTONICS

Material	n_2 $(10^{-18}\text{m}^2\text{/W})$	Nonlinear Parameter (/W/m)	Propagation Loss(dB/cm)	β_{TPA} (cm/GW)	FOM	CMOS-BEOL compatibility	ref
HNLF	2.6×10^{-2}	0.01~0.02	~0	negligible	>>1	No	[11,55,56]
Hydex	0.115	0.233	0.06	negligible	>>1	Yes	[57]
Si-Ge	9.6~11.2	25	1.4	1.16~1.5	0.53	Yes	[58]
c-Si	14.5	588	18	0.6	1.56	Yes	[59]
a-Si	21	1200	6.9	0.25	5	Yes	[60]
Si_3N_4	0.25	1	0.014	negligible	>>1	Yes	[28]
SRN	1.61	16	1.5	negligible	>>1	Yes	[47,62]
As_2Se_3	23	98	<0.001	negligible	>>1	No	[62]
As_2S_3	2.9	100	10	6.2×10^{-4}	>>1	No	[63]
AlGaAs	19.8	10~600	1.2~6	negligible	>>1	No	[61,64]
USRN	28	~280	4.5	negligible	>>1	Yes	This work

well phase matching ($\kappa \approx 0$), can be approximately expressed as: $G_s(L) \approx \cosh(gL) + \exp(-i(\phi_{rel}))\sinh(gL)$, where parametric gain coefficient $g = \sqrt{r^2 - (\kappa/2)^2}$ and $r = 2\gamma\sqrt{P_1 P_2}$ [52]. The product of the parametric gain coefficient g and nonlinear media length L directly control how much GER is achieved. To highlight the nonlinear properties of the Si_7N_3 waveguide we utilized, Table I lists the typical nonlinear parameters on various platforms, where the nonlinear figure of merit (FOM) computed as FOM $= n_2/(\lambda\beta_{TPA})$ is used to quantify the nonlinear efficiency. As intuitively obtained from the table, the drawback of the silicon-based waveguide is its relatively low nonlinear FOM due to the presence of nonlinear losses associated with the TPA and FCA. HNLFs as a medium for early nonlinear studies is not conducive to future integrated all-optical signal processing systems owing to the inferiority of low nonlinear coefficients, large size, and inevitable SBS phenomena. In comparison, Hydex, Si_3N_4 and SRN have a nonlinear FOM >> 1, nevertheless, due to their low nonlinear parameter γ, longer interaction lengths (in the orders of meters) tend to be required in order to achieve larger nonlinear phase shifts. While materials such as AlGaAs exhibit very good nonlinear properties at telecom wavelengths, they typically require a high-temperature annealing step to minimize linear losses, which makes them unsuitable for backend-of-line (BEOL) fabrication. And unless heterogeneous integration technologies are deployed, there is practically inability to bridge the gap between ultra-high nonlinear of AlGaAs and complementary metal-oxide semiconductor (CMOS) compatible platforms [60]. Finally, Si_7N_3-based nonlinear platform is potential candidate for all-optical integrated signal processing in terms of nonlinear coefficient, loss, FOM, TPA, and CMOS-BEOL compatibility. Above all, Si_7N_3 waveguide has a very great potential in realizing phase regeneration of PDM signal based on phase-sensitive amplification.

IV. CONCLUSION

In conclusion, we propose and demonstrate a scheme for phase regeneration of PDM signal based on vector dual-pump nondegenerate PSA in Si_7N_3 waveguide. Specifically, an integrated, black-box-operated vector PSA scheme is first designed while avoiding polarization diversity structures, followed by dispersion design of Si_7N_3 waveguide in which the phase-sensitive process occurs, and subsequently the performance of phase regeneration is characterized in detail based on the proposed theoretical model of optical wave transmission in the waveguide. The phase regeneration of the PDM DPSK and PDM QPSK signal is successfully performed by 1×10^7 bits data simulation, allowing the EVM of the two modulation formats to be improved from 54% and 53.78% to 13.64% and 13.64%, and from 28.87% and 29.25% to 13.72% and 13.93%, respectively. Meanwhile, the excellent phase regeneration tolerance of the proposed system is also verified. With the growing maturity of photonic integration technology, the proposed scheme will provide a promising perspective in applications such as integrated all-optical signal processing and extending the transmission distance of PDM signal in optical network.

REFERENCES

[1] S. G. Evangelides, L. F. Mollenauer, J. P. Gordon, and N. S. Bergano, "Polarization multiplexing with solitons," *J. Lightw. Technol.*, vol. 10, no. 1, pp. 28–35, Jan. 1992, doi: 10.1109/50.108732.

[2] Z.-Y. Chen et al., "Use of polarization freedom beyond polarization-division multiplexing to support high-speed and spectral-efficient data transmission," *Light Sci. Appl.*, vol. 6, no. 2, Feb. 2017, Art. no. e16207, doi: 10.1038/lsa.2016.207.

[3] Y. Frignac et al., "Transmission of 256 wavelength-division and polarization-division-multiplexed channels at 42.7Gb/s (10.2Tb/s capacity) over 3/spl times/100km of TeraLight/spl trade/fiber," in *Proc. Opt. Fiber Commun. Conf. Exhibit.*, 2002, Paper FC5, doi: 10.1109/OFC.2002.1036776.

[4] F. Yaman and G. Li, "Nonlinear impairment compensation for polarization-division multiplexed WDM transmission using digital backward propagation," *IEEE Photon. J.*, vol. 1, no. 2, pp. 144–152, Jul. 2010, doi: 10.1109/JPHOT.2009.2028157.

[5] I. Morita, K. Tanaka, N. Edagawa, and M. Suzuki, "40 Gb/s single-channel soliton transmission over transoceanic distances by reducing Gordon-Haus timing jitter and soliton-soliton interaction," *J. Lightw. Technol.*, vol. 17, no. 12, pp. 2506–2512, Dec. 1999, doi: 10.1109/50.809669.

[6] M. Nakazawa, T. Yamamoto, and K. Tamura, "1.28 Tbit/s-70 km OTDM transmission using third- and fourth-order simultaneous dispersion compensation with a phase modulator," *Electron. Lett.*, vol. 36, no. 24, pp. 2027–2029, Nov. 2000, doi: 10.1049/EL:20001391.

[7] J. Wang, S. He, and D. Dai, "On-chip silicon 8-channel hybrid (de)multiplexer enabling simultaneous mode- and polarization-division-multiplexing," *Laser Photon. Rev.*, vol. 8, no. 2, pp. 18–22, Feb, 2014, doi: 10.1002/lpor.201300157.

[8] B. Zhu et al., "112-Tb/s space-division multiplexed DWDM transmission with 14-b/s/Hz aggregate spectral efficiency over a 76.8-km seven-core fiber," *Opt. Exp.*, vol. 19, no. 17, pp. 16665–16671, Aug. 2011, doi: 10.1364/OE.19.016665.

[9] J. P. Gordon and L. F. Mollenauer, "Phase noise in photonic communications systems using linear amplifiers," *Opt. Lett.*, vol. 15, no. 23, pp. 1351–1353, Sep. 1990, doi: 10.1364/OL.15.001351.

[10] A. Demir, "Nonlinear phase noise in optical-Fiber-communication systems," *J. Lightw. Technol.*, vol. 25, no. 8, pp. 2002–2032, Aug. 2007, doi: 10.1109/JLT.2007.900888.

[11] R. Slavík et al., "All-optical phase and amplitude regenerator for next-generation telecommunications systems," *Nature Photon.*, vol. 4, no. 10, pp. 690–695, Oct. 2010, doi: 10.1038/nphoton.2010.203.

[12] K. Croussore, I. Kim, C. Kim, Y. Han, and G. Li, "Phase-and-amplitude regeneration of differential phase-shift keyed signals using a phase-sensitive amplifier," *Opt. Exp.*, vol. 14, no. 6, pp. 2085–2094, Mar. 2006, doi: 10.1364/oe.14.002085.

[13] R. Slavík et al., "Coherent all-optical phase and amplitude regenerator of binary phase-encoded signals," *IEEE J. Sel. Top. Quantum Electron.*, vol. 18, no. 2, pp. 859–869, Mar./Apr. 2012, doi: 10.1109/JSTQE.2011.2136329.

[14] J. Kakande et al., "Multilevel quantization of optical phase in a novel coherent parametric mixer architecture," *Nature Photon.*, vol. 5, no. 12, pp. 748–752, Dec. 2011, doi: 10.1038/nphoton.2011.254.

[15] K. R. H. Bottrill et al., "Full quadrature regeneration of QPSK signals using sequential phase sensitive amplification and parametric saturation," *Opt. Exp.*, vol. 25, no. 2, pp. 696–705, Jan. 2017, doi: 10.1364/OE.25.000696.

[16] B. Stiller, G. Onishchukov, B. Schmauss, and G. Leuchs, "Phase regeneration of a star-8QAM signal in a phase-sensitive amplifier with conjugated pumps," *Opt. Exp.*, vol. 22, no. 1, pp. 1028–1035, Jan. 2014, doi: 10.1364/OE.22.001028.

[17] G. Hesketh and P. Horak, "Reducing bit-error rate with optical phase regeneration in multilevel modulation formats," *Opt. Lett.*, vol. 38, no. 24, pp. 5357–5360, Dec. 2013, doi: 10.1364/OL.38.005357.

[18] Z. Tong and S. Radic, "Low-noise optical amplification and signal processing in parametric devices," *Adv. Opt. Photon.*, vol. 5, no. 3, pp. 318–384, Aug. 2013, doi: 10.1364/AOP.5.000318.

[19] C. McKinstrie and S. Radic, "Phase-sensitive amplification in a fiber," *Opt. Exp.*, vol. 12, no. 20, pp. 4973–4979, Oct. 2004, doi: 10.1364/opex.12.004973.

[20] A. Lorences-Riesgo, F. Chiarello, C. Lundström, M. Karlsson, and P. A. Andrekson, "Experimental analysis of degenerate vector phase-sensitive amplification," *Opt. Exp.*, vol. 22, no. 18, pp. 21889–21902, Sep. 2014, doi: 10.1364/OE.22.021889.

[21] A. Lorences-Riesgo, C. Lundström, F. Chiarello, M. Karlsson, and P. A. Andrekson, "Phase-sensitive amplification and regeneration of dual-polarization BPSK without polarization diversity," in *Proc. IEEE Eur. Conf. Opt. Commun.*, 2014, pp. 1–3, doi: 10.1109/ECOC.2014.6964045.

[22] W. Yang et al., "Phase regeneration for polarization-division multiplexed signals based on vector dual-pump nondegenerate phase sensitive amplification," *Opt. Exp.*, vol. 23, no. 3, pp. 2010–2020, Feb. 2015, doi: 10.1364/OE.23.002010.

[23] T. Umeki, M. Asobe, and H. Takenouchi, "In-line phase sensitive amplifier based on PPLN waveguides," *Opt. Exp.*, vol. 21, no. 10, pp. 12077–12084, May 2013, doi: 10.1364/OE.21.012077.

[24] B. J. Puttnam, D. Mazroa, S. Shinada, and N. Wada, "Phase-squeezing properties of non-degenerate PSAs using PPLN waveguides," *Opt. Exp.*, vol. 19, no. 26, pp. B131–B139, Dec. 2011, doi: 10.1364/OE.19.00B131.

[25] Y. Zhang et al., "Phase-sensitive amplification in silicon photonic crystal waveguides," *Opt. Lett.*, vol. 39, no. 2, pp. 363–366, Jan. 2014, doi: 10.1364/OL.39.000363.

[26] R. Neo et al., "Phase-sensitive amplification of light in a $\chi^{(3)}$ photonic chip using a dispersion engineered chalcogenide ridge waveguide," *Opt. Exp.*, vol. 21, no. 7, pp. 7926–7933, Apr. 2013, doi: 10.1364/OE.21.007926.

[27] J. S. Levy et al., "CMOS-compatible multiple-wavelength oscillator for on-chip optical interconnects," *Nature Photon.*, vol. 4, no. 1, pp. 37–40, Jan. 2010, doi: 10.1038/NPHOTON.2009.259.

[28] Z. Ye et al., "Overcoming the quantum limit of optical amplification in monolithic waveguides," *Sci. Adv.*, vol. 7, no. 38, Sep. 2021, Art. no. eabi8150, doi: 10.1126/sciadv.abi8150.

[29] S. Y. Siew et al., "Review of Silicon Photonics technology and Platform development," *J. Lightw. Technol.*, vol. 39, no. 13, pp. 4374–4389, Jul. 2021, doi: 10.1109/JLT.2021.3066203.

[30] K. J. A. Ooi et al., "Pshing the limits of CMOS optical parametric amplifiers with USRN: Si_7N_3 above the two-photon absorption edge," *Nature Commun.*, vol. 8, no. 1, pp. 13878–13888, Jan. 2017, doi: 10.1038/ncomms13878.

[31] T. Wang et al., "Supercontinuum generation in bandgap engineered, back-end CMOS compatible silicon rich nitride waveguides," *Laser Photon. Rev*, vol. 9, no. 5, pp. 498–506, Aug. 2015, doi: 10.1002/lpor.201500054.

[32] C. Lundström, Z. Tong, M. Karlsson, and P. A. Andrekson, "Phase-to-phase and phase-to-amplitude transfer characteristics of a nondegenerate-idler phase-sensitive amplifier," *Opt. Lett.*, vol. 36, no. 22, pp. 4356–4358, Nov. 2011, doi: 10.1364/OL.36.004356.

[33] P. A. Andrekson and M. Karlsson, "Fiber-based phase-sensitive optical amplifiers and their applications," *Adv. Opt. Photon.*, vol. 12, no. 2, pp. 367–428, Apr. 2020, doi: 10.1364/AOP.382548.

[34] R. Weerasuriya et al., "Generation of frequency symmetric signals from a BPSK input for phase sensitive amplification," in *Proc. Conf. Opt. Fiber Commun. Collocated Nat. Fiber Optic Engineers Conf.*, 2010, Art. no. 11306943, doi: 10.1364/OFC.2010.OWT6.

[35] T. Herr et al., "Universal formation dynamics and noise of Kerr-frequency combs in microresonators," *Nature Photon.*, vol. 6, no. 7, pp. 480–487, Jul. 2012, doi: 10.1038/nphoton.2012.127.

[36] T. Herr et al., "Temporal solitons in optical microresonators," *Nature Photon.*, vol. 8, no. 2, pp. 145–152, Dec. 2014, doi: 10.1038/nphoton.2013.343.

[37] Z. Lu er al., "Synthesized soliton crystals," *Nature Commun.*, vol. 12, no. 1, pp. 1–7, May 2021, doi: 10.1038/s41467-021-23172-2.

[38] R. Tang, P. Devgan, V. S. Grigoryan, and P. Kumar, "Inline frequency-non-degenerate phase-sensitive fibre parametric amplifier for fibre-optic communication," *Electron. Lett.*, vol, vol. 41, no. 19, pp. 1072–1074, Sep. 2005, doi: 10.1049/el:20052681.

[39] K. Croussore and G. Li, "Phase regeneration of NRZ-DPSK signals based on symmetric-pump Phase-sensitive amplification," *IEEE Photon. Technol. Lett.*, vol. 19, no. 11, pp. 864–866, Jun. 2007, doi: 10.1109/LPT.2007.897501.

[40] G. P. Agrawal, *Nonlinear Fiber Optics*, 6th ed. Amsterdam, The Netherlands: Elsevier Press, 2019.

[41] D. F. Edwards and E. Ochoa, "Infrared refractive index of silicon," *Appl. Opt.*, vol. 19, no. 24, pp. 4130–4131, Dec. 1980, doi: 10.1364/AO.19.004130.

[42] B. J. Frey, D. B. Leviton, and T. J. Madison, "Temperature-dependent refractive index of silicon and germanium," *Proc. SPIE*, vol. 6273, 2006, Art. no. 62732J, doi: 10.1117/12.672850.

[43] Q. Lin, O. J. Painter, and G. P. Agrawal, "Nonlinear optical phenomena in silicon waveguides: Modeling and applications," *Opt. Exp.*, vol. 15, no. 25, pp. 16604–16644, Dec. 2007, doi: 10.1364/OE.15.016604.

[44] L. Yin, Q. Lin, and G. P. Agrawal, "Soliton fission and supercontinuum generation in silicon waveguides," *Opt. Lett.*, vol. 32, no. 4, pp. 391–393, Feb, 2007, doi: 10.1364/OL.32.000391.

[45] C. Lundström, B. Corcoran, M. Karlsson, and P. A. Andrekson, "Phase and amplitude characteristics of a phase-sensitive amplifier operating in gain saturation," *Opt. Exp.*, vol. 20, no. 19, pp. 21400–21412, Sep. 2012, doi: 10.1364/OE.20.021400.

[46] J. W. Choi, B.-U. Sohn, G. F. R. Chen, D. K. T. Ng, and D. T. H. Tan, "Broadband incoherent four-wave mixing and 27 dB idler conversion efficiency using ultra-silicon rich nitride devices," *Appl. Phys. Lett.*, vol. 112, no. 18, Apr. 2018, Art. no. 181101, doi: 10.1063/1.5010841.

[47] X. Wang et al., "Silicon/silicon-rich nitride hybrid-core waveguide for nonlinear optics," *Opt. Exp.*, vol. 27, no. 17, pp. 23775–23784, Aug. 2019, doi: 10.1364/OE.27.023775.

[48] M. Gao, T. Inoue, T. Kurosu, and S. Namiki, "Evolution of the gain extinction ratio in dual-pump phase sensitive amplification," *Opt. Lett.*, vol. 37, no. 9, pp. 1439–1441, May 2012, doi: 10.1364/OL.37.001439.

[49] C. M. Caves, "Quantum limits on noise in linear amplifiers," *Phys. Rev. D*, vol. 26, no. 8, pp. 1817–1839, Oct. 1982, doi: 10.1103/PhysRevD.26.1817.

[50] R. Schmogrow et al., "Error vector magnitude as a performance measure for advanced modulation formats," *IEEE Photon. Technol. Lett.*, vol. 24, no. 1, pp. 61–63, Jan. 2012, doi: 10.1109/LPT.2011.2172405.

[51] C. Xie, "WDM coherent PDM-QPSK systems with and without inline optical dispersion compensation," *Opt. Exp.*, vol. 17, no. 6, pp. 4815–4823, Mar. 2009, doi: 10.1364/OE.17.004815.

[52] P. Dong, C. Xie, L. Chen, L. L. Buhl, and Y.-K. Chen, "112-Gb/s monolithic PDM-QPSK modulator in silicon," *Opt. Exp.*, vol. 20, no. 26, pp. B624–B629, Dec. 2012, doi: 10.1364/OE.20.00B624.

[53] J.-Y. Yang, Y. Akasaka, and M. Sekiya, "Optical phase regeneration of multi-level PSK using dual-conjugate-pump degenerate phase-sensitive amplification," in *Proc. 38th Eur. Conf. Exhib. Opt. Commun.*, 2012, Paper P3.07, doi: 10.1364/ECEOC.2012.P3.07.

[54] M. E. Marhic, *Fiber Optical Parametric Amplifiers, Oscillators and Related Devices*. Cambridge, U.K.: Cambridge Univ. Press, 2007.

[55] L. Grüner-Nielsen et al., "A silica based highly nonlinear fibre with improved threshold for stimulated brillouin scattering," in *Proc. IEEE 36th Eur. Conf. Exhib. Opt. Commun.*, 2010, pp. 1–3, doi: 10.1109/ECOC.2010.5621232.

[56] X. Feng et al., "Dispersion controlled highly nonlinear fibers for all-optical processing at telecoms wavelengths," *Opt. Fiber Technol.*, vol. 16, no. 6, pp. 378–391, Dec. 2010, doi: 10.1016/j.yofte.2010.09.014.

[57] M. Ferrera et al., "Low-power continuous-wave nonlinear optics in doped silica glass integrated waveguide structures," *Nature Photon.*, vol. 2, no. 12, pp. 737–740, Nov. 2008, doi: 10.1038/nphoton.2008.228.

[58] K. Hammani et al., "Optical properties of silicon germanium waveguides at telecommunication wavelengths," *Opt. Exp.*, vol. 21, no. 14, pp. 16690–16701, Jul. 2013, doi: 10.1364/OE.21.016690.

[59] H. Yamada et al., "Nonlinear-optic silicon-nanowire waveguides," *Jpn. J. Appl. Phys.*, vol. 44, no. 9A, pp. 6541–6545, Sep. 2005, doi: 10.1143/JJAP.44.6541.

[60] C. Grillet et al., "Amorphous silicon nanowires combining high nonlinearity, FOM and optical stability," *Opt. Exp.*, vol. 20, no. 20, pp. 22609–22615, Sep. 2012, doi: 10.1364/OE.20.022609.

[61] M. Pu et al., "Ultra-efficient and broadband nonlinear AlGaAs-on-insulator chip for low-power optical signal processing," *Laser Photon. Rev*, vol. 12, no. 12, Dec. 2018, Art. no. 1800111, doi: 10.1002/lpor.201800111.

[62] R. Ahmad and M. Rochette, "High efficiency and ultra broadband optical parametric four-wave mixing in chalcogenide-PMMA hybrid microwires," *Opt. Exp.*, vol. 20, no. 9, pp. 9572–9580, Apr. 2012, doi: 10.1364/OE.20.009572.

[63] S. Serna et al., "Engineering third-order optical nonlinearities in hybrid chalcogenide-on-silicon platform," *Opt. Lett.*, vol. 44, no. 20, pp. 5009–5012, Oct. 2019, doi: 10.1364/OL.44.005009.

[64] C. Lacava, V. Pusino, P. Minzioni, M. Sorel, and I. Cristiani, "Nonlinear properties of AlGaAs waveguides in continuous wave operation regime," *Opt. Exp.*, vol. 22, no. 5, pp. 5291–5298, Mar. 2014, doi: 10.1364/OE.22.005291.